Rare Met.
https://doi.org/10.1007/s12598-025-03491-9

RARE METALS

ORIGINAL ARTICLE

Flexible QLED array with mechanical force modulation of electroluminescence intensity

Ye-Pei Mo, Yue Liu, Li Zhang, Xin-Gang Pan, Zhi-Wei Fu*, Wen-Chao Gao*, Rong-Rong Bao*, Cao-Feng Pan*

Received: 17 April 2025 / Revised: 8 June 2025 / Accepted: 14 June 2025

Abstract Functional signal conversion devices are critical components of next-generation intelligent systems, driving an urgent demand for novel sensing materials and functionalities to enable advanced applications in intelligent robotics and human–machine interfaces. In this work, we present a quantum dot light-emitting diode (QLED) array based on a newly developed signal conversion functional material 20% Gd-doped CeO_{2-x} (CGO). Under pressure and electric field induction, the oxygen vacancy dynamics in CGO were modulated, resulting in macroscopic polarization charges, reflecting the mechanical force-electrical response effect. The QLED pixel emission intensity was controlled by external pressure, achieving a remarkable 1000% enhancement at 1.8 GPa. Combined with resolution-tunable Si MWs array, mapping of 2D pressure distribution on external objects with optical signals was realized. This work extends the force-electrical-optical signal conversion mechanism to centrosymmetric cubic fluorite materials, overcoming the traditional limitations of piezo-phototronic devices that rely on specific crystal symmetries, and provides new avenues for the development of the next-generation smart sensing.

Keywords Tactile sensing; Light emission modulation; Force electro-optical coupling

Supplementary Information The online version contains supplementary material available at https://doi.org/10.1007/s12598-025-03491-9.

Y.-P. Mo, Y. Liu, L. Zhang, W.-C. Gao*
Beijing Institute of Nanoenergy and Nanosystems, Chinese Academy of Sciences, Beijing 101400, China
e-mail: gaowenchao@binn.cas.cn

Y.-P. Mo, X.-G. Pan, R.-R. Bao, C.-F. Pan
School of Nanoscience and Engineering, University of Chinese Academy of Sciences, Beijing 100049, China

X.-G. Pan, Z.-W. Fu*
Xuzhou B&C Chemical Co. Ltd, Jiangsu 221300, China
e-mail: david@bcpharma.com

R.-R. Bao*, C.-F. Pan*
Institute of Atomic Manufacturing, Beihang University, Beijing 100191, China
e-mail: baorongrong@buaa.edu.cn

C.-F. Pan
e-mail: pancaofeng@buaa.edu.cn

R.-R. Bao, C.-F. Pan
International Institute for Interdisciplinary and Frontiers, Beihang University, Beijing 100191, China

1 Introduction

Tactile sensing is a critical mechanism for humans to perceive and interact with external environment [1–3]. Similarly, in artificial intelligence (AI) systems, replicating tactile sensing fundamentally involves converting external stimuli such as pressure and strain into analyzable optical or electrical signals [4–7]. Thus, emulating human-like tactile perception is a core challenge in AI technology [8, 9] and remains one of the key researching focuses [10–13]. With the rapid development of intelligent technology, applications such as smart robots [2, 14, 15], human–machine interfaces [3], and personalized healthcare systems [16–18] are evolving toward higher sophistication, miniaturization, and enhanced functionality [19–22], which requires their integration with tactile sensing elements with high resolution, easy to acquire signals and low cross talk [23]. Recent studies have extensively explored electrical pressure sensors for tactile sensing [24–26]. Through

Published online: 06 August 2025

innovative structural designs and functional material modifications, these sensors have evolved from single configurations to complex architectures [27–29], leading to significant improvements in important performance parameters such as dynamic response range, sensitivity, and response time [27, 30–34]. However, critical challenges persist, including difficulty in fabricating large-area array devices, limited spatial resolution in array configurations, challenges in achieving real-time pressure visualization and precise pressure mapping.

Mechanoluminescent phosphor-based sensing devices represent an attractive breakthrough in force visualization technology, enabling direct conversion of mechanical stimuli into optical signals with dynamic pressure responsiveness [35–38]. However, the spatial resolution of such devices is fundamentally limited by phosphor particle dimensions and their underlying working mechanism. In contrast, materials capable of mechanical force-electrical signal conversion demonstrate greater potential for tactile sensing applications [39, 40]. Notably, piezoelectric materials such as ZnO and GaN, which are highly responsive to mechanical stimuli, have been extensively utilized in high-resolution piezoelectric light-emitting diode (LED) arrays and thoroughly investigated in prior studies [41–44].

Interestingly, due to advancements in materials research, mechanically responsive materials are no longer confined to traditional non-centrosymmetric crystals. Even centrosymmetric materials have been engineered to exhibit mechanical response through external stimulation or doping strategies [45, 46]. This has certainly broadened the range of candidate materials for further research on mechanical force-electrical coupled devices. While the mechanisms underlying the piezoelectric properties of these centrosymmetric oxides have been discussed in detail, their application in sensing remains largely unexplored. Here, we report a QLED array with mechanical force-electrical responsiveness for high-resolution accurate optical two-dimensional (2D) pressure mapping. By introducing CGO as a mechanical force responsive functional layer, the regulation of the Schottky barrier at the metal–semiconductor interface was achieved [46], in which the piezoelectric polarization potential of CGO was used as a 'gate' to control the light emission intensity of the pixels in QLED array ultimately achieves the two-dimensional pressure distribution mapping of the shape of the external postage stamp. Under a pressure of 1.8 GPa, the pressurized pixels exhibit a remarkable 1000% enhancement in emission intensity. Furthermore, the pixel array's scalability and resolution are enabled by a flexible structural design and Si wafer-based micro/nanoprocessing. Crucially, our device combined a CGO functional layer with a flexible Si-based process to incorporate CGO into a tactile sensing array based on optical signals. This technology will broaden the application scope and multidisciplinary crossover possibilities of materials with mechanical force-electrical coupling effects and has potential applications in soft robotics, electronic skin, and high-resolution opto-electronic systems.

2 Experimental

2.1 Fabrication process for CGO films

Firstly, bottom Al electrode was deposited on cleaned Si wafer with 300 nm-thick oxide layer by magnetron sputtering (PVD75, Kurt J. Lesker) at 60 W. Subsequently, CGO films with different doping concentrations were deposited on the bottom electrode at a deposition power of 150 W for 35 min, and finally the top Ag electrode was deposited on the CGO film.

2.2 Fabrication process for Si MWs

The highly doped p-Si wafers were cleaned with acetone and ethanol to remove surface impurities, respectively. Next, the wafers were cleaned and dried with deionized water, followed by plasma treatment to improve the hydrophilicity of the wafer surface. Subsequently, a negative photoresist (HTA116, HTA112, B&C Chemicals) was spin-coated on the wafers surface (4000 rpm for 60 s) and the photoresist with the array pattern was obtained by pre-baking at 110 °C for 60 s, exposing for 12 s and post-baking at 110 °C for 60 s. This photoresist pattern was used as a mask for inductively coupled plasma (ICP) reactive ion etching (ULVAC NE-550H) to obtain a Si MWs array with a pitch of 15 μm and a size of 15 μm × 55 μm.

2.3 Fabrication process for SPCL

After obtaining wafers with regular Si MWs array, oxygen plasma treatment was performed to improve the hydrophilicity of the array. polydimethylsiloxane (PDMS) (curing agent 1:10) was then poured onto the wafer and rotated to fill the gaps of the Si microwires (MWs) (2000 rpm, 30 s). Immediately afterward, it was cured in an oven at 80 °C for 4 h. After curing, the PDMS would tightly wrap the Si MWs array to make the top of the array a continuous plane, and then the entire Si MWs arrays were cut off from the wafer together with the PDMS to obtain the complete large-area Si MWs array/PDMS composite layer (SPCL).

2.4 Fabrication process for QLED

Quantum dots (QDs) solutions were spin-coated on the surface of the SPCL (2000 rpm, 30s), followed by drying at 60 °C for 20 min to remove the solvent and obtain the QDs layer. Then CGO was deposited on the surface of the QDs layer (150 W, 35 min) as the ETL and Ag (60 W, 8 min) were deposited on the backside of the SPCL as the bottom electrode. Finally, the whole film was adhered to the ITO/PET substrate with the CGO surface, where the ITO was in contact with the CGO surface and served as the top electrode.

2.5 Characterization and measurement of the QLED array

The morphology of Si MWs array and QLED were characterized by field-emission scanning electron microscopy (SU1510, Hitachi). The QLED array was powered by a direct current (DC) source meter (M8812, Maynuo), and the EL spectra of QLEDs were measured by with spectrometer (QE65000, Ocean Optics). *I–V* and *I–T* characteristics were measured by the semiconductor device analyzer (B1500A, KEYSIGHT).

3 Results and discussion

3.1 Force-electric coupling phenomena in CGO films

Researchers have made significant advances in developing mechanical force-electrical coupled functional materials, including piezoelectric ZnO nanostructures, piezoresistive materials, and related piezoelectric systems [47]. Among these, ZnO-based materials have gained particular attention for force sensing applications due to their excellent compatibility with micro/nanofabrication processes. The piezoelectric potential generated by the deviation of the central charge under pressure can effectively modulate carrier transport characteristics in the p–n junction or the heterointerfaces, enabling external force detection through localized electrical or optical signal variations [48, 55]. Historically, research on piezoelectric materials was constrained to naturally non-centrosymmetric crystals due to fundamental structural requirements. However, recent breakthroughs in doping strategies and defect engineering have enabled the emergence of force-electrical coupling effects in centrosymmetric semiconductors. This expansion of viable material systems opens new possibilities for cross-disciplinary applications and novel device scenarios.

A conceptual schematic of the flexible mechanical force-electrical coupling responsive QLED is shown in Fig. 1A, demonstrating the potential for reflecting input mechanical signals in the form of optical signals. The operational principle relies on piezoelectric polarization-induced modulation of the local Schottky barrier at the CGO interface. Under combined electrical and mechanical stimulation, the CGO layer generates polarization charges that alter the barrier characteristics [46]. This modulation produces spatially varying current densities across the pixel array, resulting in corresponding changes in electroluminescence (EL) intensity that accurately map the pressure distribution from external objects. To investigate the force-electrical coupling characteristics of CGO thin films, we developed a custom characterization system (Fig. 2A) comprising two three-dimensional (3D) displacement stages for sample positioning, a dynamometer for applying and measuring controlled vertical pressure and a semiconductor test system for real-time electrical property measurements. The enlarged view showed the specific device structure, with a Si wafer with a SiO_2 layer as the substrate, Ag and Al as the upper and lower electrodes to form different Schottky barrier, and a layer of SiO_2 sputtered on the edge of the CGO film to act as an insulating layer to avoid short-circuiting of the top and bottom electrodes. Figure 2B–D shows the behavior of current versus pressure for CGO films with doping concentrations of 0, 10%, and 20% in the same pressure range. Notably, the pressure response exhibits progressive enhancement with increasing doping concentration, as evidenced by the systematically amplified current modulation at 1 V bias (Fig. 2E). This trend is quantitatively captured by the pressure-dependent current variation rate, providing clear evidence for doping optimized force-electrical coupling. At doping concentration of 0, the conductivity of CGO films was low, where the concentration of oxygen vacancies (V_o) was at a low level, whereas the similar radii of Gd^{3+} and Ce^{4+} ions and the lower binding energy of Gd^{3+} and Ce^{4+} result in higher conductivity of Gd_2O_3-doped CeO_{2-x} [49, 50]. The electric field-induced redistribution of mobile charges in the thin films leads to a crystalline phase transition of the material, which is associated with chemical swelling and material heterogeneity [49–52]. The presence of V_o in oxide materials can be stabilized and controlled by selecting different aliquot dopants and co-doping, which induces the redistribution of mobile V_o under electric field, resulting in the manifestation of piezoelectricity in the intrinsically centrosymmetric, non-stoichiometric oxides [46, 53]. The chemical expansion, phase transition, diffusion and redistribution of mobile ionic species in centrosymmetric ionic materials were controlled using electric fields to produce a macroscopic piezoelectric effect in the materials [46] which further modulates the Schottky barrier at the interface between the CGO and the metal electrode (Fig. 2G). Figure 2F presents the $I-T$ curves of the films

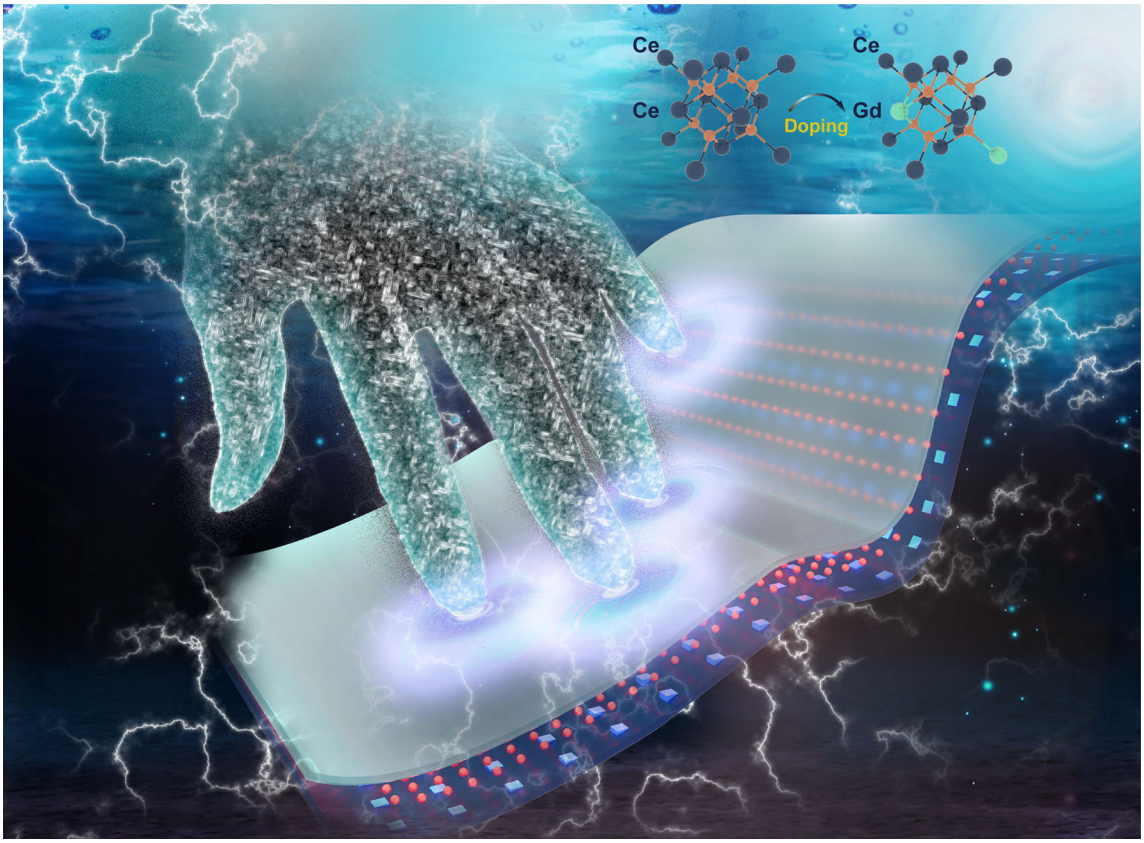

Fig. 1 Conceptual schematic illustration of a flexible mechanical force-electrical coupling responsive QLED array

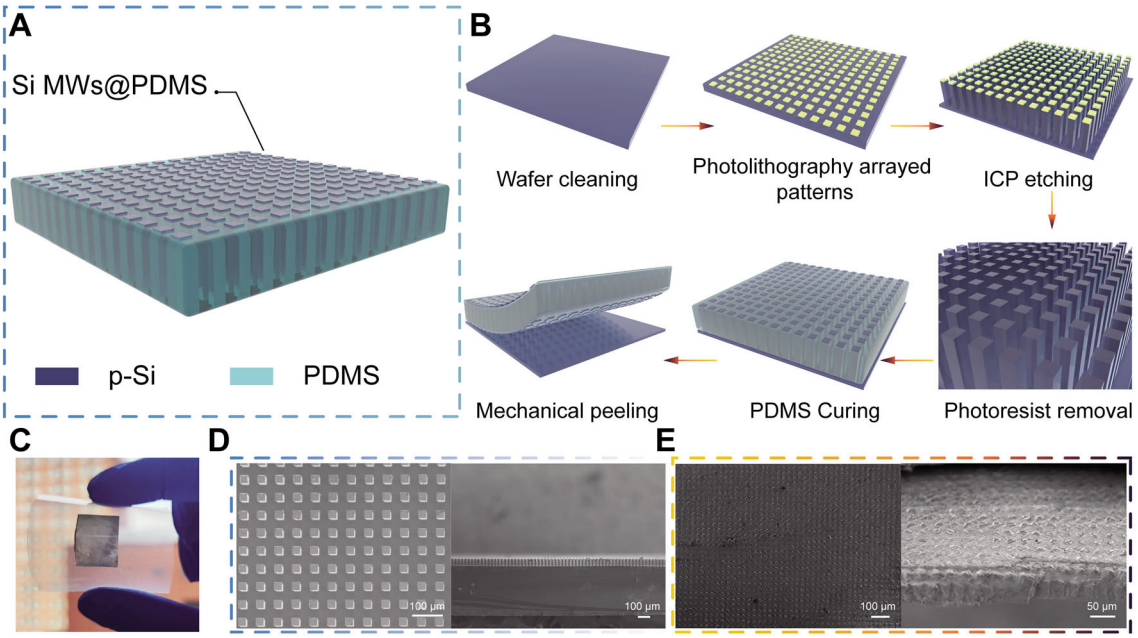

Fig. 2 Fabrication process and morphological characterization of flexible Si MWs array. **A** Schematic structure of SPCL. **B** ICP etching process utilizing photoresist as a mask and PDMS curing. **C** Optical photograph of SPCL adhered to a flexible substrate after peeling off. **D** Top and cross-sectional SEM image of a Si MWs array. **E** Top and cross-sectional SEM image of SPCL

with three doping concentrations in response to pressure, and the current of the films responds well to the loading and unloading of pressure at a fixed voltage.

3.2 Flexibility of Si microwires array

To facilitate QLED array integration and enhance mechanical force sensitivity, we incorporated a flexible p-Si microwires (MWs) array into the device architecture. Figure 3A illustrates the key structural element, that a SPCL formed by encapsulating the Si MWs array in PDMS. The fabrication process of SPCL is shown in Fig. 3B. First, photoresist was spin-coated on the cleaned highly doped p-Si, and photoresist with array pattern was obtained by UV exposure; photoresist patterns were used as a mask. After the ICP etching and cleaning process, neatly aligned array of Si MWs was obtained (Fig. S1), with individual Si MW having edge lengths and heights of 15 and 55 μm, respectively, and a pitch of 15 μm, which resulted in array of Si MWs with a resolution of up to 846 DPI and regular alignment on the surface of Si wafer (Fig. 3D), as demonstrated in the experimental section with specific process parameters. The mixed PDMS was then poured onto the surface of the Si wafer with Si MWs array and spin-coated, which would fill the gaps of the Si MWs array and leave a layer of PDMS film, following cured in an oven at 80 °C for 4 h. The curing process resulted in a coplanar PDMS surface aligned precisely with the Si MWs top (Fig. 3E), maintaining electrical contact accessibility while preventing interlayer short circuits. This precise surface control enabled clean mechanical release of the composite structure using a precision blade, yielding large-area, flexible SPCL membranes with excellent structural integrity. The optical photograph (Fig. 3C) confirms the

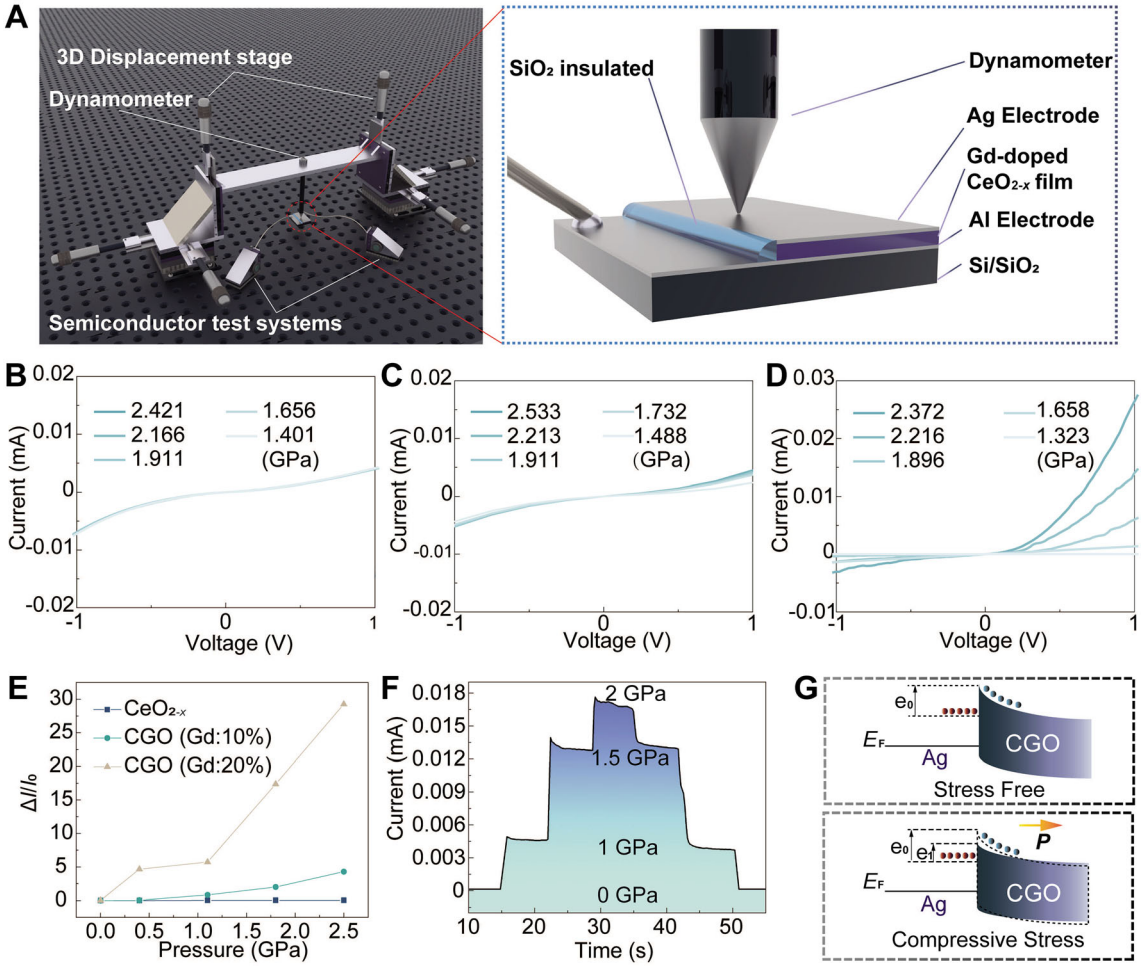

Fig. 3 Electromechanical characterization and testing device for CGO films. **A** Test device for applying pressure, consisting of a 3D displacement table, a dynamometer, and a semiconductor tester. The inset was a schematic of the test. Variation of current with pressure in **B** 0%, **C** 10%, and **D** 20% doped CGO films. **E** Rates of change of current with pressure for different doping concentrations of CGO over the same pressure range. **F** Pressure response curve of 20% doped CGO film at 0.5 V fixed voltage. **G** Modulation of Schottky barrier at metal–semiconductor interfaces by piezoelectric polarization charges

SPCL's uniform adhesion to flexible substrates, demonstrating its suitability for flexible device integration.

3.3 Optical and electrical characterization of QLED array

We further combined the SPCL prepared in the previous section with CGO to construct a flexible QLED array based on CGO and Si MWs. In the structure of QLED array (Fig. 4A), SPCL acted as the hole transport layer (HTL) and CGO as the electron transport layer (ETL). QDs were employed as the light-emitting layer because of its high optical performance, adjustable light-emitting band gap, and adaptable to different shapes of substrate [54]. Furthermore, the emission wavelength of the QLED array can be tuned by varying the QD size and composition, enabling customized optoelectronic properties for diverse applications. The fabrication process of the QLED array is shown in Fig. S2, in which a layer of QDs was spin-coated on the SPCL and a 20%-doped CGO film was deposited on top of it, then the CGO side was contacted with the PET with an ITO layer to make the ITO layer serve as the top electrode, and finally the backside of the SPCL was deposited with the Ag layer as the bottom electrode. Complete fabrication details including deposition parameters and processing conditions are provided in the experimental section. Thanks to the arrayed Si MWs HTL, the electrons could not move in the plane of the QDs layer, and thus the arrayed luminescence could be realized even if the QDs layer without pixels (Fig. 4B). Combined with the mature micro/nanofabrication process, pixels of QLED array with different morphologies and sizes could be easily obtained to meet different application requirements. Figure 4C and D represents the EL spectra with increasing voltage and turn-on voltage of the QLED, respectively. The EL peak of QLED was centered at 625 nm, which corresponds to the photoluminescence (PL) peak of QDs (Fig. S3). The absence of additional spectral features indicates high-purity emission from the QDs layer. And rectification curves of the device showed the turn-on voltage at 4 V. The device exhibited well isolated pixels with a center-to-center spacing of 30 μm. As demonstrated in Fig. 4E, individual pixels show excellent optical isolation with negligible inter-pixel cross talk. Figure 4F presents the energy-level alignment diagram of all functional layers in the QLED structure, illustrating the charge transport mechanisms.

3.4 Force-electricity-optical coupling mechanism in QLED array

To investigate the mechano-optoelectronic coupling in the QLED array, we developed a custom testing platform (Fig. 5A) that exploits the force-electrical response of CGO to modulate pixel emission. The QLED array was

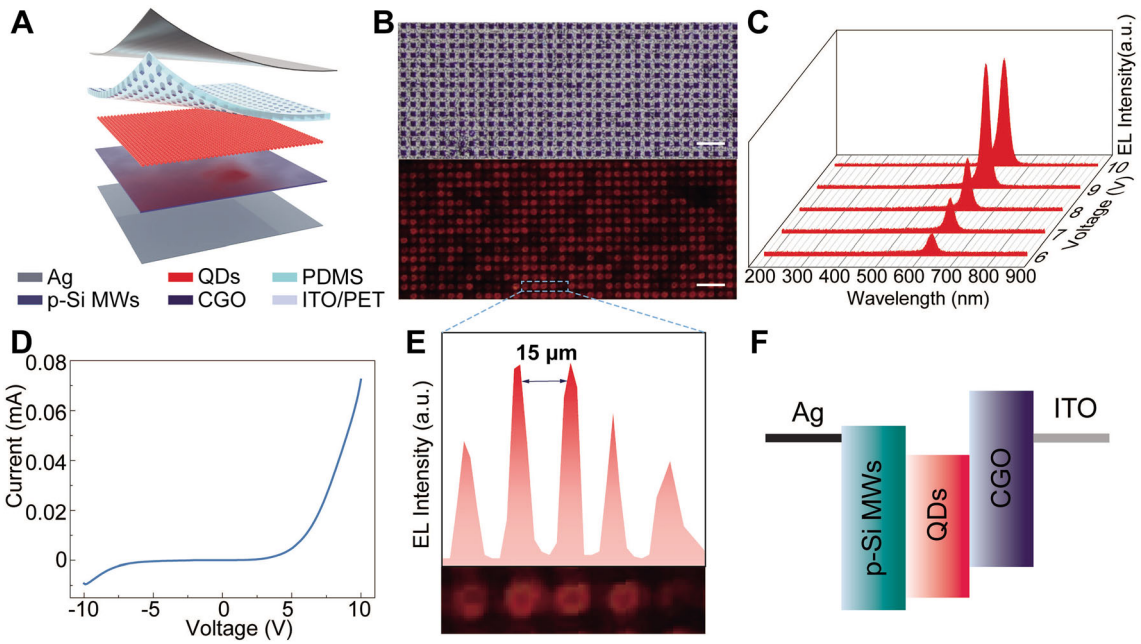

Fig. 4 Optical and electrical characterization of QLED devices. **A** Schematic structure of QLED device. **B** Each pixel could be easily distinguishable in a CCD image viewed under a microscope, including the QLED array pixels and their images when they were illuminated, and the scale bar is 100 μm. **C** EL spectra of the QLED device at different voltages. **D** Turn-on voltage of the QLED devices. **E** Enlarged view of the six illuminated pixels in **B** and the spatial resolution of the pixels. **F** Energy-level structure diagram of each layer in QLED

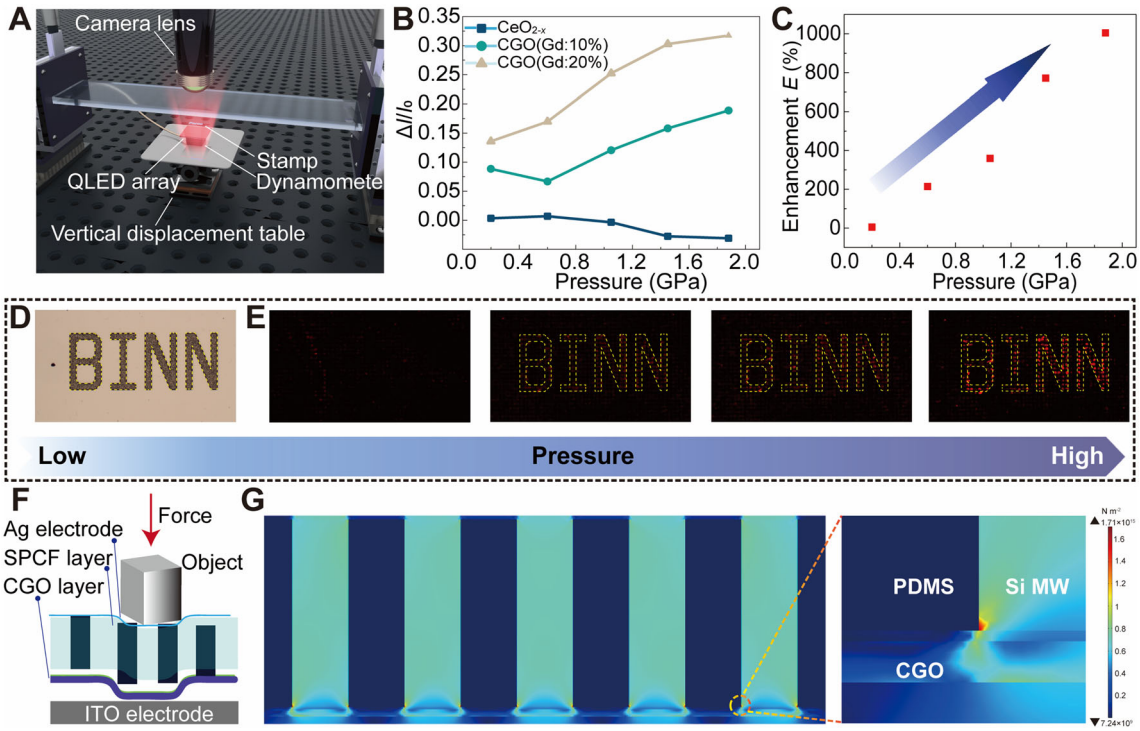

Fig. 5 Characterization of optoelectronic signals enhanced by piezoelectric effect. **A** Optical signal enhancement acquisition device consisting of CCD, displacement stage, and dynamometer. **B** Rates of change of current with pressure for QLED devices based on different doping concentrations of CGO over the same pressure range. **C** Enhancement factor *E* of QLED pixels as a function of an applied pressure of up to 1.8 GPa. **D** Si stamp with the convex character 'BINN'. **E** Process of change of luminescence intensity of pixel array under external pressure. **F** Schematic representation of the condition of each layer of the thin film when the top of the device was pressed. **G** Simulation of the stress concentration distribution inside the device under stress obtained by COMSOL

provided with controlled pressure by the vertical displacement stage rising and falling at the bottom, while the transparent acrylic plate was fixed at the top, and the optical information was captured by the charge coupled device (CCD) at the top through the transparent acrylic plate, there was a Si stamp with the convex character 'BINN' between the dynamometer and the QLED array. It could be concluded from Fig. 5B that the rate of change of the current of the devices in the same pressure range was consistent with the pattern of the rate of change of the current of the CGO in Fig. 2E, which indicated that the responsiveness to the pressure in the QLED device were determined by the CGO, and the degree of responsiveness were increased with the CGO doping concentration increased. Since the Ag electrode is in contact with the flexible SPCL, the pressurized object will inevitably cause some effects on the Ag electrode under high pressure, which may induce some microcracks and lead to the decrease of current in the undoped CeO_{2-x} film. In contrast, the 10% and 20% Gd-doped CGO films have higher conductivity, effectively compensating for electrode interface effects. This further confirms that Gd^{3+} doping significantly the electrical properties of CeO_{2-x} film. The curves represented by three doping concentrations of CGO were characterized in the uniform pressure range, which excluded the impact brought by the variation of the electrode contact area. Our analysis reveals that the applied pressure and electric field induce piezoelectric polarization in the CGO layer, which effectively modulates the Schottky barrier between CGO and ITO interface (Fig. S4). This barrier modification facilitates enhanced carrier transport across the interface, leading to significantly increased device current. In the equivalent circuit of device, the CGO was equivalent to a transistor connected in series with the QLED to control the current (Fig. S5), which serves as both an ETL and a force-electric response functional material. Similar device structures were discussed in detail in previous work [43]. When the vertical displacement stage rises, the pressure on the QLED array gradually increases, in which the luminescence intensity of the pixels increases with the increase of the current. As demonstrated in Fig. 5C, the EL intensity enhancement factor *E* of the pixels exhibits an approximately linear trend within the pressure range of 0–1.8 GPa, which was modulated by the piezoelectric polarization potential, reaching a 1000% increase at maximum pressure compared to the initial luminescence intensity. The enhancement factor was defined as $E = (I_\varepsilon - I_o)/I_o$, where I_o and I_ε were the

luminescence intensity of the pixel under zero and under applied pressure, respectively. The 2D mapping of pressure was demonstrated using the convex character 'BINN' in Fig. 5D, and the convex character was obtained by ICP etching on Si. The pressure mapping process (Fig. 5E) reveals that the EL intensity of pixels subjected to pressure was gradually increased, while the non-pressurized pixels maintain constant emission. The difference in EL intensity between pixels was gradually obvious as the pressure increased, and finally a pixel array display consistent with the Si convex character pattern was obtained. Figure 5F illustrates the mechanical deformation of the QLED array when subjected to external pressure, demonstrating stress transfer from the Si MWs array to the CGO functional layer. The simulation results of the stress in Fig. 5G reveal that when subjected to pressure, the structure of the Si MWs array would cause the stress to be concentrated in the part of the Si MWs that was connected to the QDs layer and the CGO film, the height uniformity of the Si MWs array ensures that the pressure is uniformly distributed in each Si MW and the CGO film, and complete mechanical isolation of non-pressurized regions. Uniform array structures of the Si MWs offered QLED with variable-resolution light-emitting pixels, while ensuring the CGO's response to mechanical stimuli as well as the functionality and reliability of SPCL, further demonstrating the technology's potential for integration with tactile sensing and other interfaces.

4 Conclusion

In summary, we demonstrated a mechanically responsive QLED array leveraging the unique properties of CGO and SPCL, which enables the modulation of EL intensity through external pressure. The QLED exhibits a remarkable pressure-dependent enhancement in light emission intensity, achieving a 1000% increase in EL intensity at 1.8 GPa compared to initial state. This special behavior originates from the mechanoelectronic coupling response of CGO, which allows them to modulate the height of the Schottky barrier in response to electric field and pressure, thus affecting the luminous intensity of pixels in QLED. In addition, Si MWs were obtained by UV lithography precision etching processes, yields well-defined Si MWs array with controllable pixel dimensions, enabling QLED array to have a resolution of up to 846 DPI. Furthermore, the process of preparing flexible SPCL is expected to advance the integration of Si-based materials into flexible sensing technologies. This work provides a viable approach for the stress expansion of centrosymmetric oxides and manipulation of the luminescent properties of centrosymmetric oxide semiconductor-based QLED by applying static strains, and can be linked to other interfacial effects, showing extraordinary potential for applications in the fields of haptic sensors, MENS, and artificial intelligence.

Acknowledgements This work was financially supported by the National Natural Science Foundation of China (Nos. 52192610, 62422120, 52371202, 52125205, and 52250398), the Natural Science Foundation of Beijing Municipality (No. L223006), Shenzhen Science and Technology Program (No. KQTD20170810105439418) and the Fundamental Research Funds for the Central Universities. The authors also thank Xuzhou B&C Chemical Co., Ltd for providing the photoresist (HTA116 and HTA112, B&C Chemicals) used in our work.

Author contributions Ye-Pei Mo contributed to investigation, writing original draft, conceptualization, and methodology. Yue Liu contributed to investigation, conceptualization, and review. Li Zhang, Zhi-Wei Fu and Xin-Gang Pan contributed to investigation and review. Wen-Chao Gao contributed to project administration. Rong-Rong Bao and Cao-Feng Pan contributed to funding acquisition and project administration.

Data availability The data that support the findings of this study are available from the corresponding author upon reasonable request.

Declarations

Conflict of interests Cao-Feng Pan is an editorial board member for *Rare Metals* and was not involved in the editorial review or the decision to publish this article. All authors declare that there are no competing interests.

References

[1] Liu Y, Bao RR, Tao J, Li J, Dong M, Pan CF. Recent progress in tactile sensors and their applications in intelligent systems. Sci Bull. 2020;65(1):70–88. https://doi.org/10.1016/j.scib.2019.10.021.

[2] Bao RR, Tao J, Zhao J, Dong M, Li J, Pan CF. Integrated intelligent tactile system for a humanoid robot. Sci Bull. 2023;68(10):1027–37. https://doi.org/10.1016/j.scib.2023.04.019.

[3] Wu WQ, Wang CF, Han ST, Pan CF. Recent advances in imaging devices: image sensors and neuromorphic vision sensors. Rare Met. 2024;43(11):5487–515. https://doi.org/10.1007/s12598-024-02811-9.

[4] Wen DP, Chen P, Liang Y, Mo XM, Pan CF. Regulated polarization degree of upconversion luminescence and multiple anti-counterfeit applications. Rare Met. 2024;43(5):2172–83. https://doi.org/10.1007/s12598-024-02675-z.

[5] Liu Y, Xu HY, Dong M, Han RH, Tao J, Bao RR, Pan CF. Highly sensitive wearable pressure sensor over a wide sensing range enabled by the skin surface-like 3D patterned interwoven structure. Adv Mater Technol. 2022;7(12):2200504. https://doi.org/10.1002/admt.202200504.

[6] Liu Y, Tao J, Yang W, Zhang Y, Li J, Xie H, Bao RR, Gao WC. Pan CF biodegradable, breathable leaf vein-based tactile sensors with tunable sensitivity and sensing range. Small. 2022;18(8):e2106906. https://doi.org/10.1002/smll.202106906.

[7] Zhao SF, Ran WH, Wang LL, Shen GZ. Interlocked MXene/rGO aerogel with excellent mechanical stability for a health-monitoring device. J Semicond. 2022;43(8):082601. https://doi.org/10.1088/1674-4926/43/8/082601.

[8] Han BJ, Han ZW, Ying T, Hao Z, Li YS, Shen MJ. Mesoscopic model construction and mechanical response of carbon nanotube

reinforced magnesium matrixcomposites. Chin J Rare Met. 2024;48(06):833–42. https://doi.org/10.13373/j.cnki.cjrm.XY23030040.
[9] Chen CJ, Zhao SL, Pan CF, Zi YL, Wang FC, Yang C, Wang ZL. A method for quantitatively separating the piezoelectric component from the as-received "Piezoelectric" signal. Nat Commun. 2022;13(1):1391. https://doi.org/10.1038/s41467-022-29087-w.
[10] Wang CF, Hu HJ, Zhu DL, Pan CF. Mechanoluminescence-powered bite-controlled human–machine interface. Sci Bull. 2023;68(6):559–61. https://doi.org/10.1016/j.scib.2023.02.036.
[11] Xu SM, Fan XJ, Chen SY, Manshaii F, Yin JY, Chen J. Advances in luminescent fibers for interactive smart textiles. cMat. 2024;1(3):e33. https://doi.org/10.1002/cmt2.33.
[12] Zhou QT, Deng SJ, Gao AL, Wang BY, Lai JX, Pan J, Huang L, Pan CF, Meng GW, Xia F. Triboelectric nanogenerator with dynamic electrode for geological disaster and fall-down self-powered alarm system. Adv Funct Mater. 2023;33(52):2306619. https://doi.org/10.1002/adfm.202306619.
[13] Zhou KK, Zhao Y, Sun XP, Yuan ZQ, Zheng GQ, Dai K, Mi LW, Pan CF, Liu CT, Shen CY. Ultra-stretchable triboelectric nanogenerator as high-sensitive and self-powered electronic skins for energy harvesting and tactile sensing. Nano Energy. 2020;70:104546. https://doi.org/10.1016/j.nanoen.2020.104546.
[14] Zheng JX, Zhou ZA, Feng T, Li H, Sun CH, Wang N, Tian Y, Zhao Y, Zhou SY. Hydrophobic long-chain two-dimensional perovskite scintillators for underwater X-ray imaging. Rare Met. 2024;43(1):175–85. https://doi.org/10.1007/s12598-023-02421-x.
[15] Yao Y, Chen Q, Li YQ, Huang XH, Ling WW, Xie ZM, Wang JQ, Chen CM. Nanodiamond/Ti_3C_2 MXene-coated quartz crystal microbalance humidity sensor with high sensitivity and high quality factor. Rare Met. 2024;43(6):2719–29. https://doi.org/10.1007/s12598-023-02564-x.
[16] Zhang YF, Lu QC, He J, Huo ZH, Zhou RH, Han X, Jia MM, Pan CF, Wang ZL, Zhai JY. Localizing strain via micro-cage structure for stretchable pressure sensor arrays with ultralow spatial crosstalk. Nat Commun. 2023;14(1):1252. https://doi.org/10.1038/s41467-023-36885-3.
[17] Xu MX, Dou C, Song TY, Li X, Zhang Q. A temperature-insensitive silver nanostructures@graphene foam for high accuracy and full range human health monitoring. Rare Met. 2024;43(11):5953–63. https://doi.org/10.1016/j.nanoen.2021.106700.
[18] Yang WK, Liu H, Du HY, Zhang MY, Wang CF, Yin R, Pan CF, Liu CT, Shen CY. Robust and superelastic spider web-like polyimide fiber-based conductive composite aerogel for extreme temperature-tolerant linear pressure sensor. Sci China Mater. 2023;66(7):2829–42. https://doi.org/10.1007/s40843-022-2418-1.
[19] Tao J, Dong M, Li L, Wang CF, Li J, Liu Y, Bao RR, Pan CF. Real-time pressure mapping smart insole system based on a controllable vertical pore dielectric layer. Microsyst Nanoeng. 2020;6(1):62. https://doi.org/10.1038/s41378-020-0171-1.
[20] Wan WQ, Liang KM, Zhu PY, Chen XY, Li ZF, Liu SY, Zhang S, Song Y, He P, Wong YH, Zhang SY. Highly stable strain sensor using rGO decorated with multi-component alloy nanoparticles for human motion monitoring. Rare Met. 2024;43(12):6486–99. https://doi.org/10.1007/s12598-024-02890-8.
[21] Li F, Wang XD, Xia ZG, Pan CF, Liu QL. Photoluminescence tuning in stretchable PDMS film grafted doped core/multishell quantum dots for anticounterfeiting. Adv Funct Mater. 2017;27(17):1700051. https://doi.org/10.1002/adfm.201700051.
[22] Hu CQ, Chai RQ, Wei ZM, Li L, Shen GZ. ZnSb/$Ti_3C_2T_x$ MXene van der Waals heterojunction for flexible near-infrared photodetector arrays. J Semicond. 2024;45(5):052601. https://doi.org/10.1088/1674-4926/45/5/052601.
[23] Wang XD, Zhang HL, Dong L, Han X, Du WM, Zhai JY, Pan CF, Wang ZL. Self-powered high-resolution and pressure-sensitive triboelectric sensor matrix for real-time tactile mapping. Adv Mater. 2016;28(15):2896. https://doi.org/10.1002/adma.201503407.
[24] Ge G, Lu Y, Qu XY, Zhao W, Ren YF, Wang WJ, Wang Q, Huang W, Dong XC. Muscle-inspired self-healing hydrogels for strain and temperature sensor. ACS Nano. 2020;14(1):218–28. https://doi.org/10.1021/acsnano.9b07874.
[25] Cong RD, Qiao S, Liu JH, Mi JS, Yu W, Liang BL, Fu GS, Pan CF, Wang SF. Ultrahigh, ultrafast, and self-powered visible-near-infrared optical position-sensitive detector based on a CVD-prepared vertically standing few-layer MoS_2/Si heterojunction. Adv Sci. 2018;5(2):1700502. https://doi.org/10.1002/advs.201700502.
[26] Zhou RR, Hu GF, Yu RM, Pan CF, Wang ZL. Piezotronic effect enhanced detection of flammable/toxic gases by ZnO micro/nanowire sensors. Nano Energy. 2015;12:588–96. https://doi.org/10.1016/j.nanoen.2015.01.036.
[27] Wu WQ, Lu H, Han X, Wang CF, Xu ZX, Han ST, Pan CF. Recent progress on wavelength-selective perovskite photodetectors for image sensing. Small Methods. 2023;7(4):2201499. https://doi.org/10.1002/smtd.202201499.
[28] He JQ, Wei RL, Ge SP, Wu WQ, Guo JC, Tao J, Wang R, Wang CF, Pan CF. Artificial visual-tactile perception array for enhanced memory and neuromorphic computations. InfoMat. 2024;6(3):e12493. https://doi.org/10.1002/inf2.12493.
[29] Han X, Xu ZX, Wu WQ, Liu XH, Yan PG, Pan CF. Recent progress in optoelectronic synapses for artificial visual-perception system. Small Struct. 2020;1(3):2000029. https://doi.org/10.1002/sstr.202000029.
[30] Wu WQ, Han X, Li J, Wang XD, Zhang YF, Huo ZH, Chen QS, Sun XD, Xu ZS, Tan YW, Pan CF, Pan AL. Ultrathin and conformable lead halide perovskite photodetector arrays for potential application in retina-like vision sensing. Adv Mater. 2021;33(9): 2006006. https://doi.org/10.1002/adma.202006006.
[31] Li X, Lin YX, Cui L, Li CN, Yang ZH, Zhao SC, Hao TL, Wang GQ, Heo JY, Yu JC, Chang YW, Zhu J. Stretchable and lithography-compatible interconnects enabled by self-assembled nanofilms with interlocking interfaces. ACS Appl Mater Interfaces. 2023;15(48):56233. https://doi.org/10.1021/acsami.3c11760.
[32] Meng JP, Li Q, Huang J, Pan CF, Li Z. Self-powered photodetector for ultralow power density UV sensing. Nano Today. 2022;43: 101399. https://doi.org/10.1016/j.nantod.2022.101399.
[33] Peng YY, Lu JF, Wang XD, Ma WD, Que ML, Chen QS, Li FT, Liu XH, Gao WC, Pan CF. Self-powered high-performance flexible GaN/ZnO heterostructure UV photodetectors with piezo-phototronic effect enhanced photoresponse. Nano Energy. 2022;94: 106945. https://doi.org/10.1016/j.nanoen.2022.106945.
[34] Cheng HR, Pan YM, Li W, Liu CT, Shen CY, Liu XH, Pan CF. Facile design of multifunctional melamine foam with Ni-anchored reduced graphene oxide/MXene as highly efficient microwave absorber. Nano Today. 2023;52:101958. https://doi.org/10.1016/j.nantod.2023.101958.
[35] Larson C, Peele B, Li S, Robinson S, Totaro M, Beccai L, Mazzolai B, Shepherd R. Highly stretchable electroluminescent skin for optical signaling and tactile sensing. Science. 2016;351(6277):1071. https://doi.org/10.1126/science.aac5082.
[36] Park D, Kim WJ, Park CY, Choi J, Ghorai A, Lee GW, Choi SM, Moon WY, Jeong UY. Interactive deformable colored sound display achieved with electrostrictive fluoropolymer and halide perovskite. Small. 2024;20(43):2402281. https://doi.org/10.1002/smll.202402281.

[37] Shin HC, Sharma BK, Lee SW, Lee JB, Choi MW, Hu LH, Park CL, Choi JH, Kim TW, Ahn JH. Stretchable electroluminescent display enabled by graphene-based hybrid electrode. ACS Appl Mater Interfaces. 2019;11(15):14222. https://doi.org/10.1021/acsami.8b22135.
[38] Qu XW, Sun XW. Impedance spectroscopy for quantum dot light-emitting diodes. J Semicond. 2023;44(9):091603. https://doi.org/10.1088/1674-4926/44/9/091603.
[39] Mo YP, Feng XL, Zhang L, Han RH, Bao RR, Pan CF. Tuning the light emission of a Si micropillar quantum dot light-emitting device array with the strain coupling effect. NPG Asia Mater. 2022;14(1):83. https://doi.org/10.1038/s41427-022-00430-3.
[40] Li XY, Chen MX, Yu R, Zhang T, Song D, Liang R, Zhang Q, Cheng S, Dong L, Pan A, Wang ZL, Zhu JY, Pan CF. Enhancing light emission of ZnO-nanofilm/Si-micropillar heterostructure arrays by piezo-phototronic effect. Adv Mater. 2015;27(30):4447. https://doi.org/10.1002/adma.201501121.
[41] Pan CF, Dong L, Zhu G, Niu SM, Yu RM, Yang Q, Liu Y, Wang ZL. High-resolution electroluminescent imaging of pressure distribution using a piezoelectric nanowire LED array. Nat Photonics. 2013;7(9):752. https://doi.org/10.1038/nphoton.2013.191.
[42] Chen MX, Pan CF, Zhang T, Li XY, Liang R, Wang ZL. Tuning light emission of a pressure-sensitive silicon/ZnO nanowires heterostructure matrix through piezo-phototronic effects. ACS Nano. 2016;10(6):6074. https://doi.org/10.1021/acsnano.6b01666.
[43] Bao RR, Wang CF, Peng ZC, Ma C, Dong L, Pan CF. Light-emission enhancement in a flexible and size-controllable ZnO nanowire/organic light-emitting diode array by the piezotronic effect. ACS Photon. 2017;4(6):1344. https://doi.org/10.1021/acsphotonics.7b00386.
[44] Xu ZS, Han X, Wu WQ, Li FT, Wang R, Lu H, Lu QC, Ge BH, Cheng NY, Li XY, Yao GJ, Hong H, Liu KH, Pan CF. Controlled on-chip fabrication of large-scale perovskite single crystal arrays for high-performance laser and photodetector integration. Light Sci Appl. 2023;12(1):67. https://doi.org/10.1038/s41377-023-01107-4.
[45] Yang MM, Luo ZD, Mi Z, Zhao JJ, E SP, Alexe M. Piezoelectric and pyroelectric effects induced by interface polar symmetry. Nature. 2020;584(7821):377. https://doi.org/10.1038/s41586-020-2602-4.
[46] Park DS, Hadad M, Riemer LM, Ignatans R, Spirito D, Esposito V, Tileli V, Gauquelin N, Chezganov D, Jannis D, Verbeeck J, Gorfman S, Pryds N, Muralt P, Damjanovic D. Induced giant piezoelectricity in centrosymmetric oxides. Science. 2022;375(6581):653. https://doi.org/10.1126/science.abm7497.
[47] Pan CF, Zhai JY, Wang ZL. Piezotronics and piezo-phototronics of third generation semiconductor nanowires. Chem Rev. 2019;119(15):9303. https://doi.org/10.1021/acs.chemrev.8b00599.
[48] Pan CF, Chen MX, Yu RM, Yang Q, Hu YF, Zhang Y, Wang ZL. Progress in piezo-phototronic-effect-enhanced light-emitting diodes and pressure imaging. Adv Mater. 2015;28(8):1535. https://doi.org/10.1002/adma.201503500.
[49] Lee HC, Kim D, Lee JA, Heo YW, Kim JJ, Lee JH. Oxygen migration energy in La and Y Co-doped CeO_2: effect of lattice constant and grain boundary segregation. J Sci Adv Mater Devices. 2022;7(3):100450. https://doi.org/10.1016/j.jsamd.2022.100450.
[50] El-Habib A, Addou M, Aouni A, Diani M, Zimou J, Bouachri M, Brioual B, Allah RF, Rossi Z, Jbilou M. Oxygen vacancies and defects tailored microstructural, optical and electrochemical properties of Gd doped CeO_2 nanocrystalline thin films. Mater Sci Semicond Process. 2022;145:106631. https://doi.org/10.1016/j.mssp.2022.106631.
[51] Lai A, Schuh CA. Direct electric-field induced phase transformation in paraelectric zirconia via electrical susceptibility mismatch. Phys Rev Lett. 2021;126(1):015701. https://doi.org/10.1103/PhysRevLett.126.015701.
[52] Khanbabaee B, Mehner E, Richter C, Hanzig J, Zschornak M, Pietsch U, Stöcker H, Leisegang T, Meyer DC, Gorfman S. Large piezoelectricity in electric-field modified single crystals of $SrTiO_3$. Appl Phys Lett. 2016;109(22):222901. https://doi.org/10.1063/1.4966892.
[53] Li XY, Liang RR, Tao J, Peng ZC, Xu QM, Han X, Wang XD, Wang CF, Zhu J, Pan CF, Wang ZL. Flexible light emission diode arrays made of transferred Si microwires-ZnO nanofilm with piezo-phototronic effect enhanced lighting. ACS Nano. 2017;11(4):3883. https://doi.org/10.1021/acsnano.7b00272.
[54] Lee B, Oh JY, Cho H, Joo CW, Yoon H, Jeong S, Oh E, Byun J, Kim H, Lee S, Seo J, Park CW, Choi S, Park NM, Kang SY, Hwang CS, Ahn SD, Lee JI, Hong Y. Ultraflexible and transparent electroluminescent skin for real-time and super-resolution imaging of pressure distribution. Nat Commun. 2020;11(1):663. https://doi.org/10.1038/s41467-020-14485-9.
[55] Dong L, Liu YC, Tong YH, Xiao ZY, Zhang JY, Lu YM, Shen DZ, Fan XW. Preparation of ZnO colloids by aggregation of the nanocrystal subunits. J Colloid Interface Sci. 2005;283(2):380–4. https://doi.org/10.1016/j.jcis.2004.09.044.